11th ANKARA INTERNATIONAL AEROSPACE CONFERENCE **AIAC-2021-069**
8-10 September 2021 - METU, Ankara TURKEY

THE NUMERICAL SOLUTION OF FLOW FIELD AROUND S76 ROTOR

Erol Aksoy* and Mehmet Sahin†
Istanbul Technical University
Istanbul, Turkey

ABSTRACT

The hover analysis using CFD tools have been gaining popularity since CFD techniques and softwares became essential tools to achieve high accuracy results on the existing complex geometries and, also, future geometries. However, solving a flow around a rotor is still very expensive due to the complex behaviours of the air flow around a rotor. This study attempts to analyze the S-76 main rotor configuration with swept-tapered tip in the hover position. The SU2 software is utilized with an adaptive mesh refinement method provided by pyAMG software in this respect. Thoroughly capture of tip vortices is aimed with a significant decrease in the number of nodes compared to studies in the literature, taking advantage of anisotropic mesh adaptation process. Three different adaptation conditions were practised in the present study. The simulation results were found very encouraging to apply anisotropic mesh adaptation when solving a rotor problem with open source tools.

INTRODUCTION

The hover performance of a helicopter is key to the efficiency of its rotor system. In this respect, some preliminary methods such as blade element theory, blade element momentum theory, free and prescribed wake methods were developed to quickly analyze the hover performance[Jain, 2016]. Although these methods are very fast, they do not directly take the viscous and nonlinear effects into account and are not applicable to complex geometries because of the simplifications made in these methods. On the other hand, CFD tools have high reliability and can calculate complex flow properties on complex geometries, although they require very high computational times compared to the simple theories mentioned above.

The flow-field around a rotor includes strong vorticities, shock formations at the tip and complex phenomenas, such as vortex-blade interaction [Hariharan and Sankar, 2000]. In addition, Hariharan and Sankar states that the vortex-wake system can easily move away from the wing, however it remains in the proximity of the body in the case of rotor flight [Hariharan and Sankar, 2000]. By adding the fact that rotors may have complicated geometries, CFD usage becomes inevitable for these types of analysis. Even if CFD tools have sufficient capabilities to capture these types of complex flow behaviours, it is still difficult to thoroughly capture tip vortices. Because the regions where

*MSc. Stu. in Aeronautics and Astronautics Engineering, Email: aksoyer16@itu.edu.tr
†Prof. in Astronautical Engineering Department, Email: msahin@itu.edu.tr

the tip-vortices occur in the flow-field requires very fine grid structures. As stated by Chaderjian, the wake grid resolution has a vital importance to capture tip vortices and, also, the grid resolution of the region under the rotor identifies the dissipation location of the wake shear layer [Chaderjian, 2012]. Unfortunately, tip vortices has certain effects on the in-flow ratio of a rotor. Therefore, thorougly capture of the tip-vortices is a must for designer to correctly predict the thrust and power values of helicopter.

There are several researches in the literature to study rotor performances, those who are interested in, can see the indicated references [Chaderjian, 2012; Jain, 2015; Narducci, 2015; Tadghighi, 2014; Jain, 2016; Abras and Hariharan, 2015]. Most of the studies were conducted on the main rotor of the S-76 helicopter because of the availability of experimental data. In the present study, the experimental study of Balch and Lombardi [Balch and Lombardi, 1985] was chosen as the benchmark study to compare the calculated values of thrust (C_T), torque (C_Q) coefficients and figure of merit (FM) parameters. The values obtained from the experimental study are shown below,

$$C_T = \frac{T}{\rho A_d V_{tip}^2} = 0.0059 \qquad C_Q = \frac{Q}{\rho A_d V_{tip}^3} = 0.000471 \qquad FM = \sqrt{\frac{C_T}{2}}\frac{C_T}{C_Q} = 0.68812.$$

where ρ, T and Q are density, thrust and torque, A_d is disk area and equals to πR^2 and V_{tip} indicates the velocity at the tip of rotor blade.

In the present study, the flow-field around the main rotor of the S-76 helicopter with swept-tapered tip geometry is simulated by using the SU2 Multi-Physics Simulation Software [Palacios, Alonso, Duraisamy, et al., 2013]. An "Adaptive Mesh Refinement (AMR)" procedure is utilised during the solution process to overcome mentioned difficulty to capture tip-vortices. A significant reduction in the grid numbers compared to the studies mentioned before is expected with the help of anisotropic adaptive mesh refinement procedure. The procedure is conducted by an anisotropic adaptive mesh refinement library "pyAMG" [PYAMG, 2018]. Although a branch of SU2 employing the pyAMG is available publicly, it is limited to steady state solutions with a limited number of sensor functions. Therefore, the pyAMG python interface is carefully modified in order to account unsteady motions with several other sensor functions. As a result, it is expected that thorugly capture of tip vortices around the rotor and predict the figure of merit value within an acceptable error range.

METHODS

The SU2 software can perform wide-variety of analysis in the form of various equations such as Navier-Stokes, RANS, Euler, etc. [Palacios, Alonso, Duraisamy, et al., 2013]. Several approaches to solve moving meshes are available in the SU2 [Palacios, Alonso, Duraisamy, et al., 2013]. They are "Rotating Frame" and "Rigid Motion" options. Rigid Motion method can solve unsteady problems by calculating velocities at each grid point by moving them. It employs Arbitrary-Lagrangian-Eulerian (ALE) type equations. On the other hand, the Rotating Frame method solves rotation problems as if they are steady although the rotation problems are unsteady by nature. It calculates velocities at each vertex by using rotational velocity about a user-defined point and modifies equations where the reference frame rotates with the body. In the present study in this paper, rigid motion (unsteady) approach is utilized because rotating frame (steady) approach may lead to wrong solutions due to the local time stepping approach of the SU2 when utilising it simultaneously with the AMR. Roe's upwind scheme [Roe, 1981] is practised to calculate convective fluxes. To achieve a second order accuracy in convective fluxes, the MUSCL method [Van Leer, 1979] is utilized. All gradient calculations are conducted using Green-Gauss method [Palacios, Alonso, Duraisamy, et al., 2013].

The main objective of this study, application of mesh refinement, provides a great opportunity to decrease time required for mesh generation and to accelerate the solution by decreasing the required

amount of elements in the computational domain while achieving better accuracy. Because it allows to refine only necessary regions in the computational domain. However, Habashi et al. [Habashi, Dompierre, Ait-Ali-Yahia, et al., 2000] states that isotropic mesh refinement methods can increase the number of elements because it carries out the refinement in all direction and creates isotropic elements. On the contrary, generally, directional refinement is needed in the refinement region, since high gradients generally occurs in one direction such as normal to the shock-wave. Therefore, an-isotropic mesh adaptation was developed. Since the FVM and FEM can theoritically work on any type of unstructured mesh, it is convenient and very beneficial to use an an-isotropic mesh adaptation with FVM and FEM. For this purpose, several libraries and tools have been developed in the literature. To do the mesh refinement in this study, the pyAMG library [PYAMG, 2018] is utilized interfacing it with the SU2. Mach number and entropy based sensor functions are used in the mesh refinement process.

Besides all of the benefits of anisotropic AMR, implementation of the method to the SU2 software to solve the flow around a rotor may includes difficult situations. Firstly, the baseline solution must be carefully done because wrong regions can be refined if vortex ring is not diffused before the adaptation process. Therefore, rotor must be allowed to run with baseline mesh without any AMR process until the removal of starting vortex ring structure. In addition, local time stepping approach of the SU2 can causes a difficulty. The SU2 practises constant CFL number on the whole domain and this number remains same during the simulation. Therefore, all elements in the computational domain have their own fictitious time step for Newton iterations. And this time step is reduced for refined regions due to the AMR. If this time step has very low values, there appear a inconsistency between fictitious and physical time steps. There are several solutions of this situation such as decreasing physical time steps, increasing Newton iterations or increasing CFL number. First two solutions have adverve effects on the speed of calculation. In this respect, CFL number of 20 is performed in the present study. The number of Newton iterations for each time step is set to 10. It also requires 1000 time steps for a single rotor revolution.

ROTOR GEOMETRY AND BASELINE COMPUTATIONAL GRID

The main rotor of S76 helicopter is a four-bladed rotor. In the present study, the rotor geometry with swept-tapered tip shape is employed. The main characteristics of the rotor are shown at Table 1. The rotor are constituted from 3 different airfoils, SC1013R8, SC1095R8 and SC1095, along the span and transition regions appear between the airfoils. The cutout location corresponds to $\%19R$. And there are $\%60$ taper and 35^o swept angle in reference to the leading edge at the tip. The rotor geometry with details including twist distribution is shown in Figure 1.

Table 1: Characteristics of the S-76 main rotor blade

Parameters	Values
Number of blades	4
Rotor solidity	0.07043
Cut-out location(%R)	19
Tip location(%R)	95
Tip taper Ratio(%)	60
Tip sweep(LE)	35
Radius(m)	6.704
Ref. chord(m)	0.371

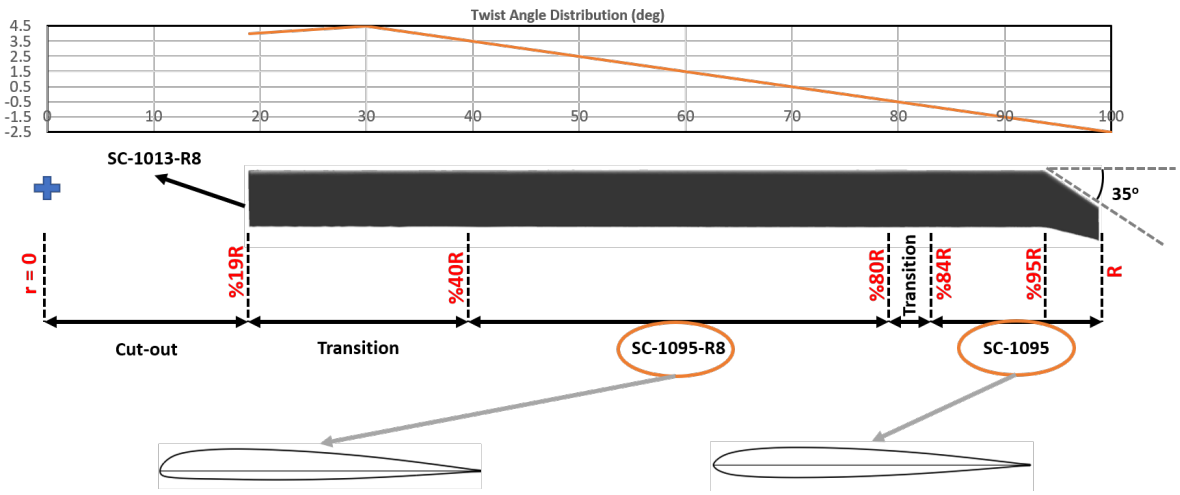

Figure 1: Rotor blade geometry.

Computational Grids

The grid generation process is one of the most important one. Because a computational grid must be consistent with flow physics. In this respect, an unstructured computational domain was created for the Euler simulation. The surface mesh of the blades and the volume mesh are examined in the following sections.

Blade Surface Mesh: Unstructured blade surface mesh is shown in Figure 2. 235 points are used along the span where the number of chord-wise vertices is 59 at the root and 44 at the tip. Span-wise points are aligned more often at the root and tip to capture the tip and root vortices. Since the blade has different airfoils and a high twist rate along the span, it is hard to capture geometry by using unstructured surface mesh from leading edge to trailing edge. Some disorders appear on the surface unless very fine surface mesh is created. To overcome this issue, boundary layer-like grid structures are created starting from the leading edge and also from the trailing edge. At the middle of the chord, these layers coming from the leading and the trailing edges become merged.

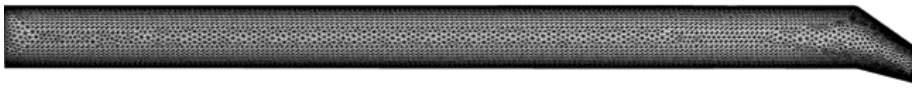

Figure 2: Blade surface mesh.

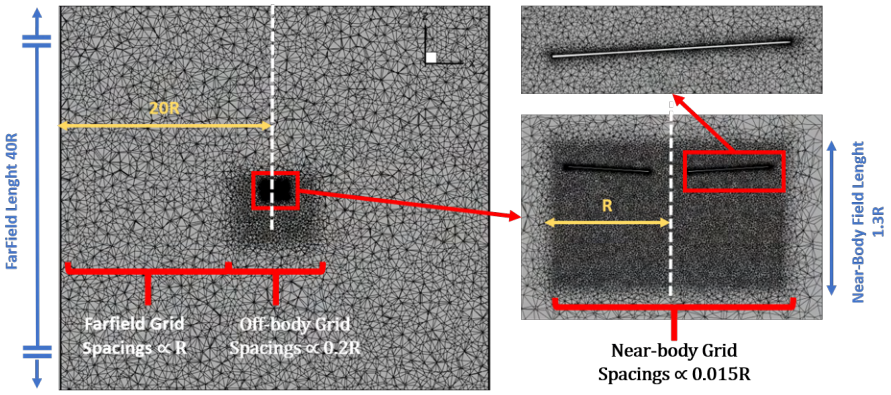

Figure 3: Computational domain of the Euler case.

Volume Mesh: The grid topology of the Euler grid can be seen in Figure 3. The spacings in this grid are enlarged step by step as moving away from the body. The near-body zone has a cylindrical shape with $1.3R$ height and $2R$ diameter. In this zone, a uniform spacing as $0.015R$ is used. The off-body zone with the spacing of $0.2R$ also indicates a cylindrical shape. However, in this time, the height of the cylinder is $5.4R$ while the diameter is $6R$. And the spacings at the farfield have the value of R where the farfield cylinder elongates $40R$ in the longitudinal direction and $40R$ in the radial direction.

ANALYSIS CONDITIONS

The main rotor of S-76 helicopter is practised with 3.5° cone angle and 9° collective pitch angle. The analysis on this rotor has 0.65 tip Mach number and 1.18 million Reynolds number based on the reference chord length. As summarized in Table 2, rigid motion method, which employs ALE type equations, was applied. Convective fluxes were calculated by utilising Roe's flux difference scheme [Roe, 1981] with MUSCL method [Van Leer, 1979]. CFL number of the simulation was held as 20 during entire simulation. And an adaptive mesh refinement methodology was practised with the help of open-source pyAMG library [PYAMG, 2018]. In general, simulation conditions for the present case are summarized in Table 2.

Table 2: Simulation conditions of the test case

Parameters	Value
Reynolds number	1.18
Tip Mach number	0.65
Cone angle	3.5°
Collective angle	9°
Solved equation	Euler
Time integration scheme	1st Order Dual-Time Stepping
Convective flux disc.	ROE Flux Difference Scheme
Baseline solution	10 Revolution
CFL number	20

Three different simulations were performed where the conditions at Table 2 are same for each. However there are differences in adaptation parameters where the refinement is conducted every 1000 iteration for all simulations. The first simulation is conducted with Mach number based sensor function and second simulation utilises entropy based sensor function. Also the third simulation uses entropy sensor, however it differs in HGRAD and adaptation size parameters from the second simulation. HGRAD parameter affects the refinement, further increasing number of nodes in the direction of high gradient and decreasing the number of nodes in the direction of low gradient. Therefore, resulting elements are formed more-stretched along the direction of low gradient. The conditions are collected at Table 3.

RESULTS AND DISCUSSION

The analysis process can be divided into two main part by considering adaptive refinement. They are baseline solution and refined solution. The baseline solution, in which the solution is conducted without any refinement, is needed to prevent solver to refine wrong locations by providing a rough solution. Since the baseline solution is same for each case, simulations mentioned in the previous section will be examined in several topics. Firstly, baseline solution will be explained. Then, each simulation will be given in different subsections.

Table 3: Adaptation parameters for simulations.

Parameters	Simulation 1	Simulation 2	Simulation 3
Sensor Function	Mach	Entropy	Entropy
HGRAD	1.2	1.2	1.3
	4 × 400000	4 × 400000	4 × 400000
Adaptation	4 × 800000	4 × 800000	3 × 800000
Size	3 × 2400000	1 × 2400000	4 × 2400000
	-	2 × 2000000	-

Baseline Solution

First 10000 iteration(10 revolution of the rotor) corresponds to the baseline solution and it does not contain a refinement process. The baseline solution is important for refinement. Because wrong regions can be refined in the absence of a good baseline solution, leading to wrong solutions. Therefore, the baseline mesh was allowed to rotate for such a number of revolutions that is sufficiently large to reduce the residuals and to diffuse the initial vortex ring. If the vortex ring structures, which can be seen in the case of Revolution 2 and 7 in Figure 4, are not removed before the refinement application, the vortex ring region can be extremely refined. Therefore, it restricts the wake region under the rotor, effecting the residuals and other parameters. To avoid this situation, the baseline solution was continued until the disappearance of the initial vortex ring, which is seen in Figure 4 where revolution 9 does not include this type of structure. In addition, by allowing the rotor to rotate for 10 revolution, it is guaranteed that the residuals, torque and thrust values reach a plateau as seen in Figure 8. It is also stated in the Ref. [Kang and Kwon, 2002] that AMR is applied after FM reaches a steady value.

(a) Revolution 2 (b) Revolution 7 (c) Revolution 9

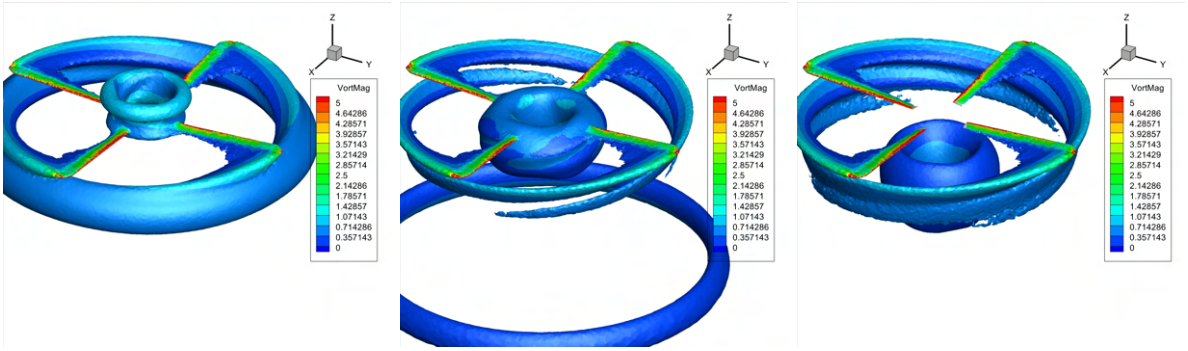

Figure 4: Tip vortices visualization for baseline solution by using iso-entropy surfaces

Simulation 1 - Mach Sensor

The simulation was allowed to run for 21 revolution in total (including baseline solution). It started with number of $1,043,679$ vertices and, at the end, the vertex number became $9,281,967$ due to the adaptive mesh refinement. The Figure 5 shows the grid structures depending on the number of revolution. In addition, the variation of number of total vertices and the number of tetrahedral elements at the boundaries depending on the refinement iterations are shown at Table 4. It can be stated that the initial mesh was refined through the wake structures because the refined regions are elongated through them and even this view of the grids in Figure 5 alone is sufficient to acquire some informations about the wake structures in a basic level. Exploiting the unstructured mesh and anisotropic mesh adaptation, the grid points are gathered tightly along the direction of higher gradients while they line up sparsely along the lower ones.

(a) Revolution 11 (1,316,518 vertex) (b) Revolution 15 (3,020,049 vertex) (c) Revolution 21 (9,281,967 vertex)

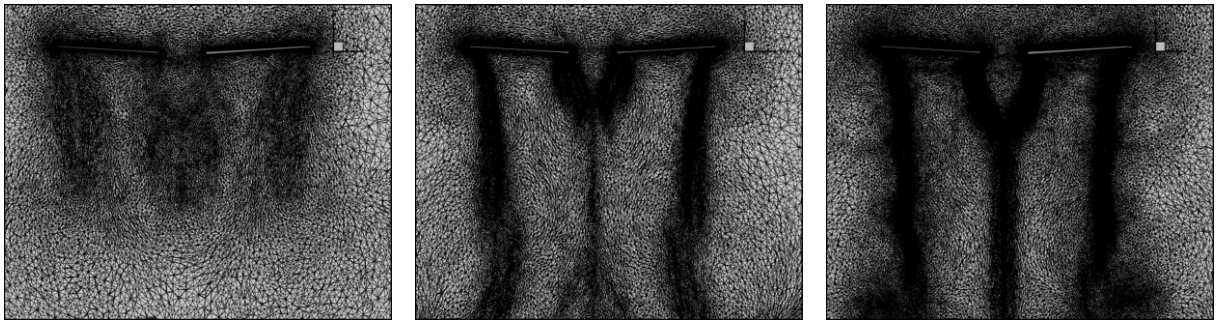

Figure 5: Wake region mesh (Side-View) visualization for simulation 1 with Mach sensor.

Table 4: Number of total vertex in computational domain and tetrahedral elements at the boundaries depending on refinement iterations for simulation 1 with Mach sensor.

		Boundary Elements	
	Total Vertex	**Rotor**	**Farfield**
ite 0	1316518	41654	1052
ite 1	1481798	35162	1032
ite 2	1651870	34392	1054
ite 3	1774167	35852	1068
ite 4	2756504	45098	1084
ite 5	3141219	50032	1128
ite 6	3384998	53394	1168
ite 7	3568984	56316	1170
ite 8	7382756	89118	1246
ite 9	8598223	99666	1230
ite 10	9281967	104294	1234

The figures of vortices seen in Figure 6 were obtained using iso-entropy surfaces. As observed, entropy can be a good indicator of vortices and wakes. In the revolution 11, the tip vortices rotates around the rotor only once. The rotation number becomes two for revolution 15. And it can be seen that there are at least 3 rotations around the rotor. This can be seen more precisely in Figure 7. In this figure entropy contours are drawn and it allows to follow the generation of tip vortex over time. The red circles indicate vortex cores in Figure 7. One, two and four vortex core formation can be observed in Figure 7 respectively for the revolutions of 11, 15 and 21.

The variations of torque and thrust coefficients are drawn in Figure 8 where each 1000 iterations correspond to one revolution. The resulting values calculated for these parameters are

$$C_T = 0.006268 \qquad C_Q = 0.000451 \qquad FM = 0.77792$$

By comparing these values to the Balch and Lombardi's experiment [Balch and Lombardi, 1985], an increase in the FM and thrust coefficients is observed whereas torque coefficient is lower than the experimental one. This is considered as a result of solving the Euler equations, since it does not include viscous effects. A numerical comparison of the performance parameters to the experimental values are available for all simulations at Table 7.

(a) Revolution 11 (b) Revolution 15 (c) Revolution 21

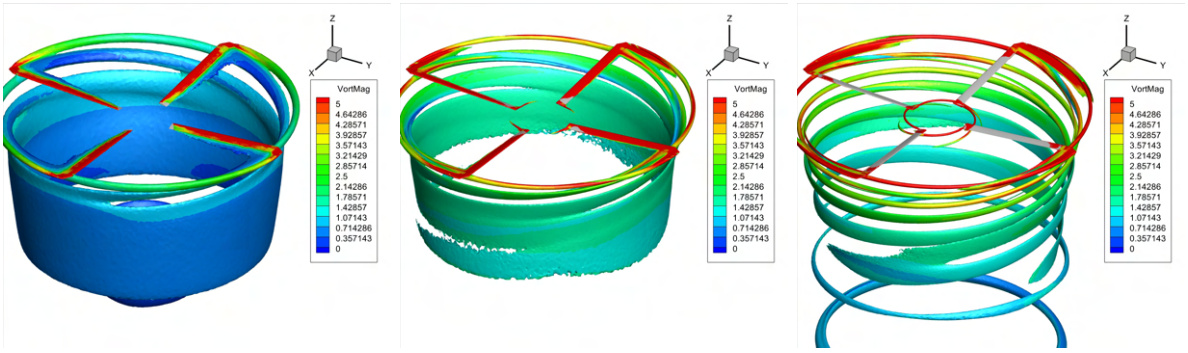

Figure 6: Tip-vortex visualization by Iso-entropy surfaces for simulation 1 with Mach sensor.

(a) Revolution 11 (b) Revolution 15 (c) Revolution 21

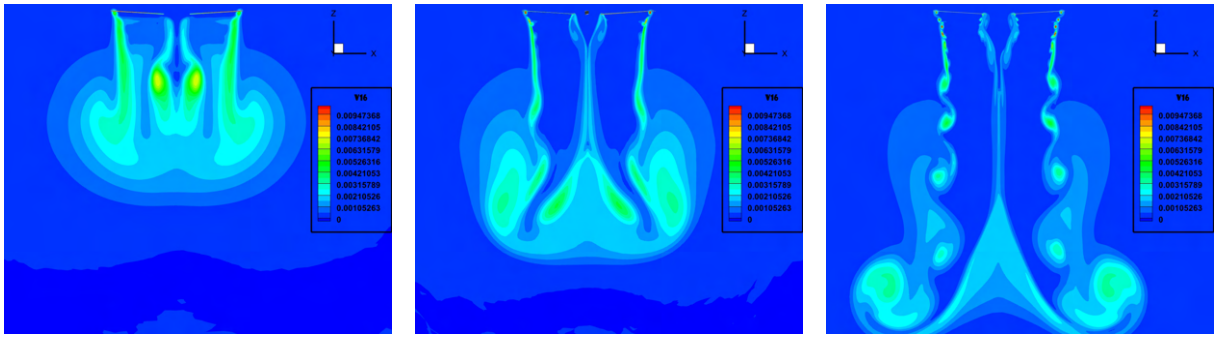

Figure 7: Wake region visualization by entropy contours for simulation 1 with Mach sensor.

(a) Tork and Thrust Coefficients (b) Residuals

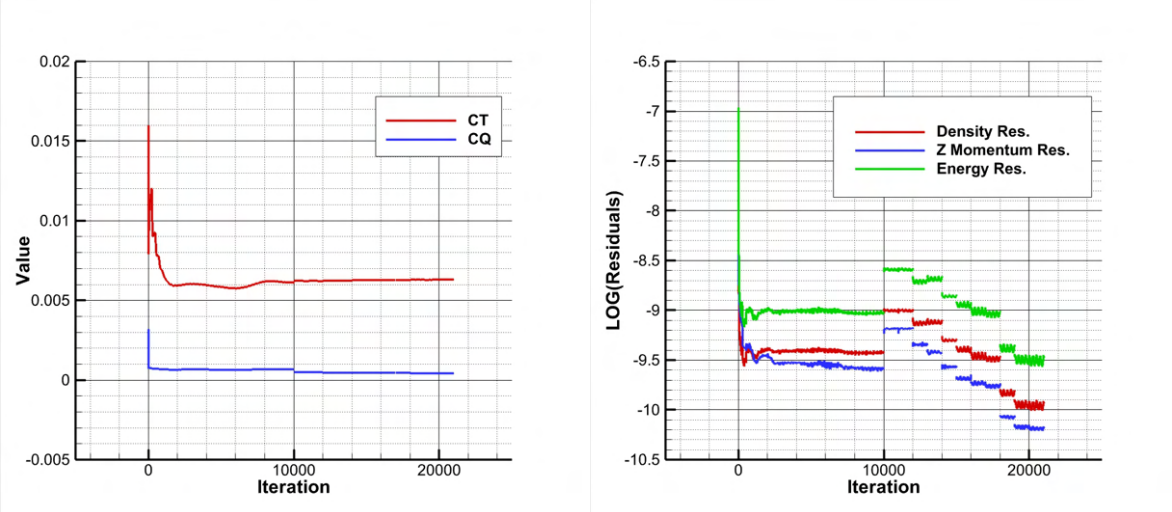

Figure 8: Variation of performance parameters of simulation 1 depending on the time iteration where every 1000 iterations correspond to one revolution.

Simulation 2 - Entropy Sensor and HGRAD 1.2

In the current analysis, the vertex number became $17,550,230$ as of revolution 21 and the variation of number of total vertices and the number of tetrahedral elements at the boundaries depending on the refinement iterations are shown at Table 5. If the vertex numbers of two simulation for the same revolution are compared, it can be said that entropy sensor causes greater vertex numbers due

to the refinement. The relative increase in the vertex numbers results from the refinement of wake layer along the rotor trailing edge.

The main outstanding difference between the Mach and the entropy sensors at first sight is that the entropy can capture the wake layer where Mach sensor could not do that. This can be seen in Figure 9. It can be seen that the wake layer is also refined in addition to the tip vortices. The entropy gradients get high values for wake layer and tip vortices, whereas the Mach gradients have lower values for wake layer. Therefore, the entropy sensor achieve better accuracy when capturing the wake layer. This brings an increase in the number of nodes, however, achieves better accuracy in FM and C_Q values than the Mach sensor.

(a) Revolution 11 (1,772,576 vertex) (b) Revolution 15 (5,833,385 vertex) (c) Revolution 21 (17,550,230 vertex)

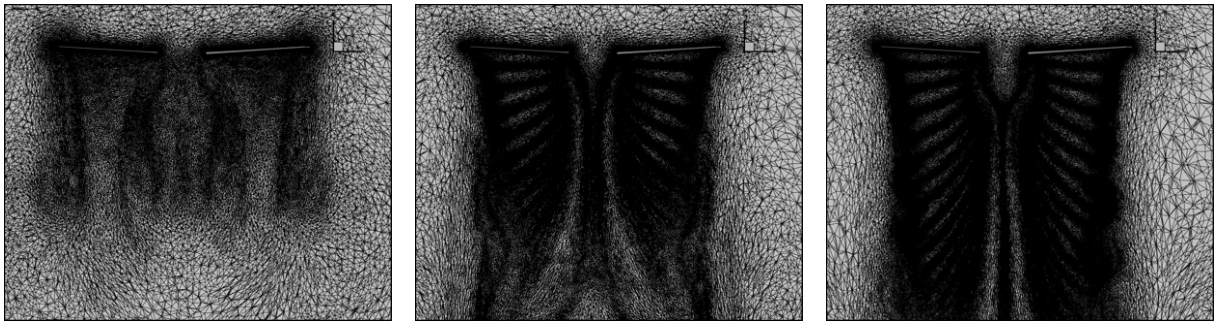

Figure 9: Wake region mesh visualization (side-view) for the simulation 2 with entropy sensor.

Table 5: Number of total vertex in computational domain and tetrahedral elements at the boundaries depending on refinement iterations for simulation 2.

		Boundary Elements	
	Total Vertex	**Rotor**	**Farfield**
ite 0	1772576	63258	982
ite 1	2464992	58118	950
ite 2	3092612	48438	990
ite 3	3683396	45006	974
ite 4	5833385	51938	992
ite 5	6921031	57410	1010
ite 6	7833217	61250	1020
ite 7	8489426	62056	1036
ite 8	14923300	82044	1086
ite 9	16289703	91162	1082
ite 10	17550230	95800	1100

In addition, entropy sensor provides better simulation of tip vortices than Mach sensor. While four vortex cores can be observed in Figure 7 for 21^{th} revolution, the vortex core number is more than seven for the 21^{th} revolution of the simulation with entropy sensor as seen in Figure 11. Therefore, the tip vortices for simulation with entropy sensor were able to be visualized as being more discrete structures, on the other hand, the tip vortices for simulation with the Mach sensor were able to be visualized as being more diffused layer-type structures. Besides, the history values for residuals, C_T and C_Q in Figure 12 showed an improvement compared to the Mach sensor.

(a) Revolution 11 (b) Revolution 15 (c) Revolution 21

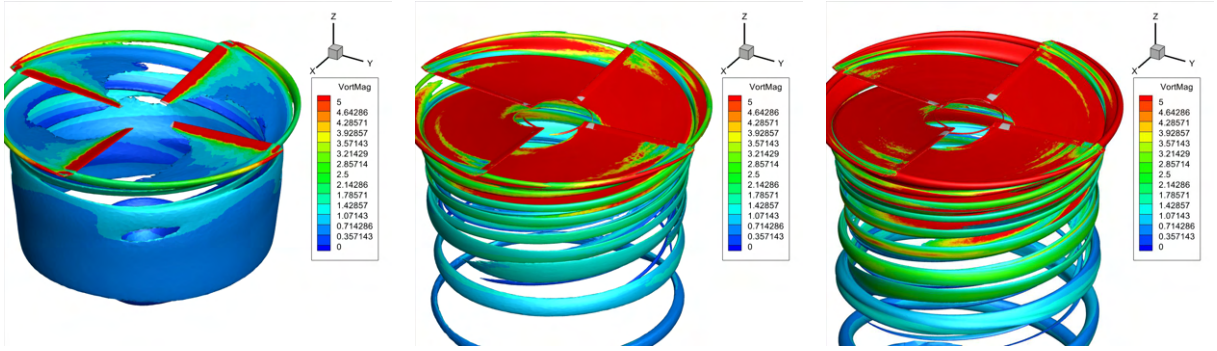

Figure 10: Tip vortices visualization by iso-entropy surfaces for the simulation 2 with entropy sensor.

(a) Revolution 11 (b) Revolution 15 (c) Revolution 21

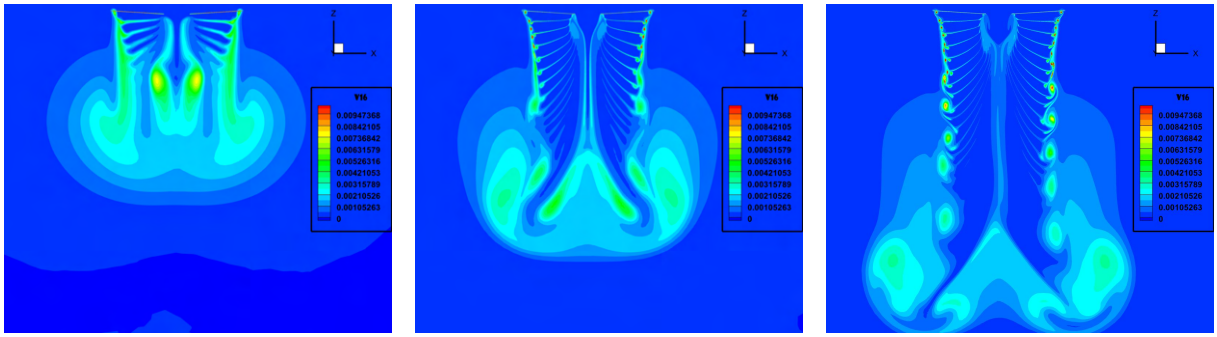

Figure 11: Wake region visualization by entropy contours for simulation 2 with entropy sensor.

(a) Torque and Thrust Coefficients (b) Residuals

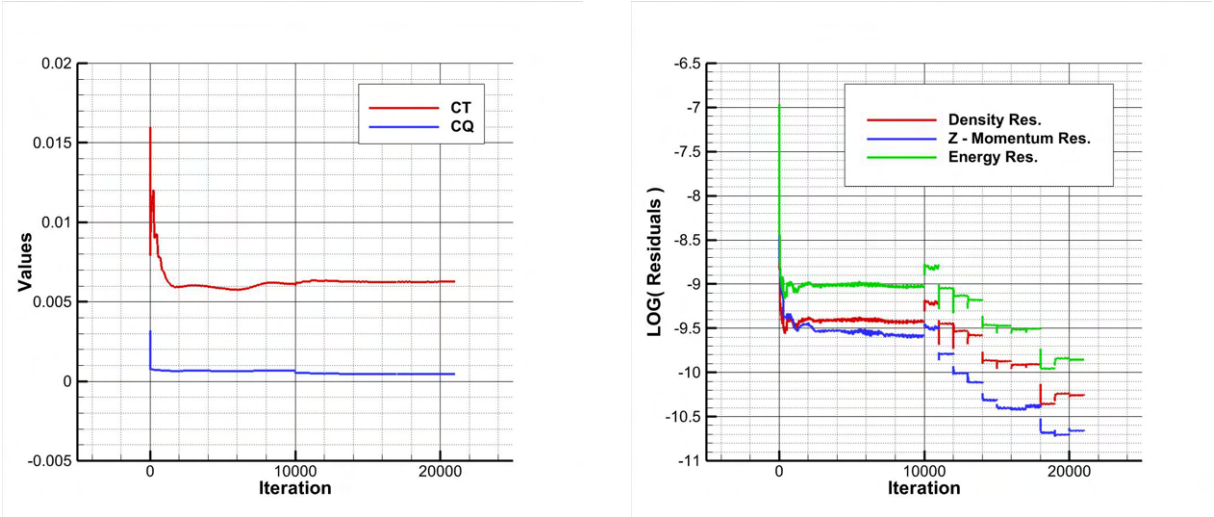

Figure 12: Variation of the analysis parameters of simulation 2 depending on the time iteration where every 1000 iterations correspond to one revolution.

The resulting values for C_T, C_Q and FM are

$$C_T = 0.006264 \qquad C_Q = 0.000461 \qquad FM = 0.76020.$$

The values shows an improvement comparing to Mach sensor calculations. However, they have still differences according to the Balch and Lombardi's experiment [Balch and Lombardi, 1985] as seen

at Table 7.

Simulation 3 - Entropy Sensor and HGRAD 1.3

The vertex number became $12,038,895$ after 21 revolution of the rotor and the variation of number of total vertices and the number of tetrahedral elements at the boundaries depending on the refinement iterations are shown at Table 6. The vertex numbers at every iterations are slightly higher than the Mach sensor, whereas a great decrease is seen comparing to the entropy sensor and HGRAD 1.2. The difference is a result of the refinement structure. The parameter of HGRAD affects the elongation of refined grid structures. High gradient directions in the flowfield are exposed to refinement in a greater amount when higher values of HGRAD are introduced. This situation creates a coarsely aligned meshes along the low gradients. Therefore, resulting highly anisotropic grid structures give layer-type structures and this analysis could capture wake shear layer better than the tip vortices.

(a) Revolution 11 (1,369,257 vertex) (b) Revolution 15 (3,749,272 vertex) (c) Revolution 21 (12,038,895 vertex)

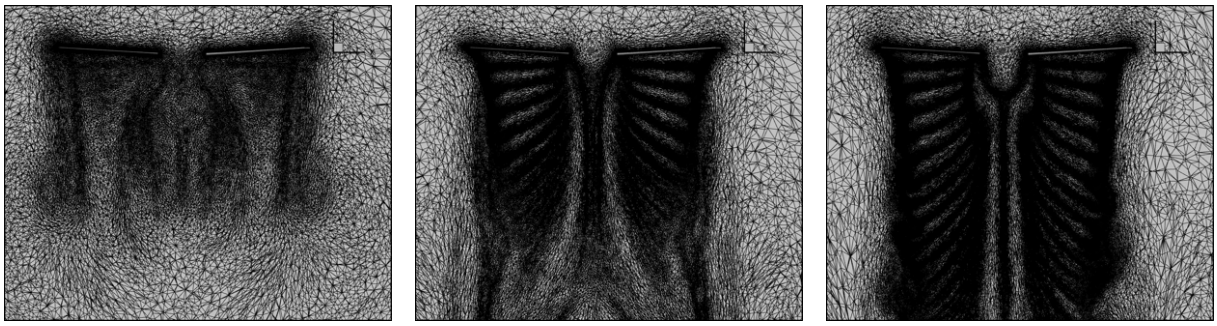

Figure 13: Wake Region Mesh (Side-View) for the simulation 3 with entropy sensor and HGRAD 1.3.

Table 6: Number of total vertex in computational domain and tetrahedral elements at the boundaries depending on refinement iterations for simulation 3.

		Boundary Elements	
	Total Vertex	**Rotor**	**Farfield**
ite 0	1369257	49786	494
ite 1	1744272	43582	488
ite 2	2049499	34082	558
ite 3	2329512	29668	588
ite 4	3749272	32810	604
ite 5	4326479	34584	600
ite 6	4699870	35320	602
ite 7	9197218	47676	618
ite 8	10759289	54614	626
ite 9	11539885	59166	622
ite 10	12038895	62180	628

Since the refinement in the current simulation focuses on the high gradient areas more than simulation 2 with HGRAD 1.2, the wake layers and root vortex region can be observed and captured more discretely as seen in Figure 13. Therefore, it provides a decrement in the number of nodes. If one compares the resulting grid structures of the simulation 2 and simulation 3, the refined regions are more compact in the case of low HGRAD values than the current simulation. For simulation 3, the

wake layer can be seen discretely up to higher distances under the rotor.

(a) Revolution 11 (b) Revolution 15 (c) Revolution 21

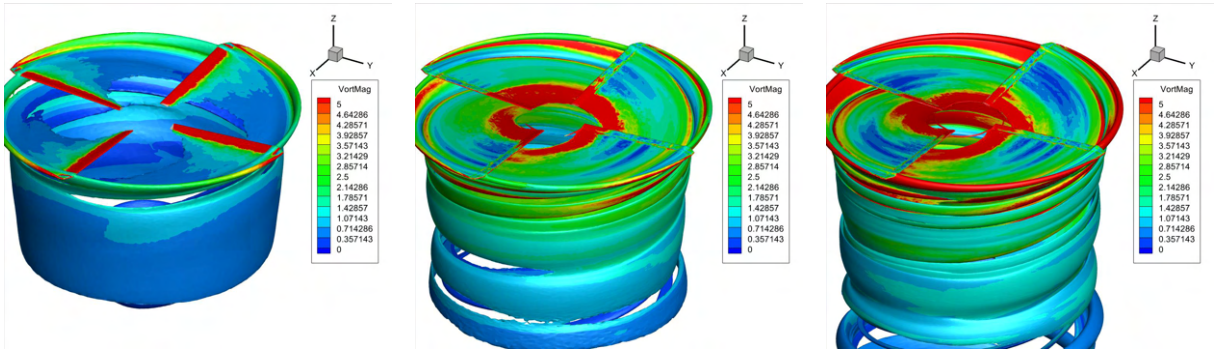

Figure 14: Tip votices visualization by iso-entropy surfaces of Simulation 3 with entropy sensor and HGRAD 1.3.

Besides, the tip vortices were captured like a shear layer, because of the high HGRAD values, as seen in Figure 14. They have smaller thickness in the radial direction and larger thickness in the vertical direction. This is more clear when the entropy contours of the simulation 2 and the simulation 3 are compared. For the simulation 2, red regions indicating vortex cores are in the shape of circles, however the red regions of simulation 3 are more like a thin layer as seen in Figure 15.

(a) Revolution 11 (b) Revolution 15 (c) Revolution 21

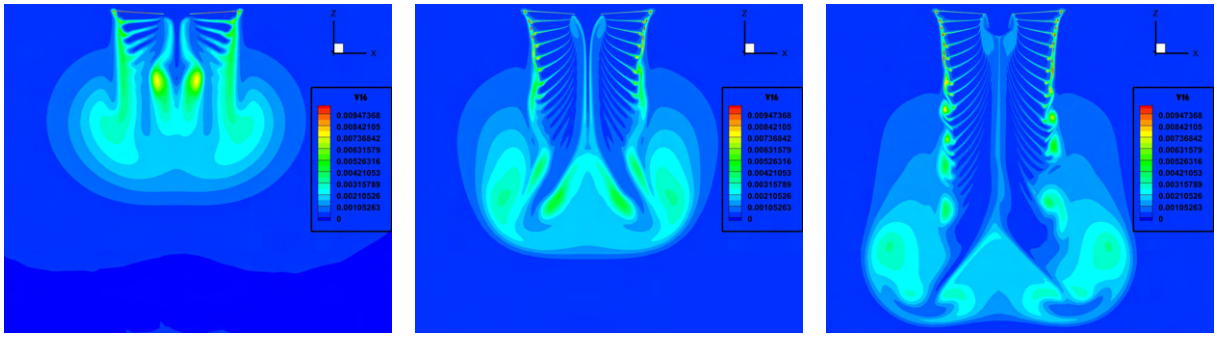

Figure 15: Wake region visualization by entropy contours of Simulation 3 with entropy sensor and HGRAD 1.3.

In addition to all of the mentioned characteristics of the current simulation, it provided the best solution for C_T, C_Q and FM. The resulting values are

$$C_T = 0.006195 \qquad C_Q = 0.000486 \qquad FM = 0.709539.$$

The values shows a great improvement comparing to Mach sensor and HGRAD 1.2 calculations. And they are very close to the values from the Balch and Lombardi's experiment [Balch and Lombardi, 1985]. The error values calculated based on the experimental results are shown at Table 7. Also, the history values of residuals and C_T, C_Q values are seen in Figure 16.

As a summary, the calculated values for performance parameters and the experimental ones [Balch and Lombardi, 1985] are compared to each other at Table 7. It is obvious that the third simulation has given most correct solutions in terms of FM. The second simulation with entropy sensor and HGRAD 1.2 followed the third simulation with entropy sensor and HGRAD 1.3. And the Mach

sensor solution showed worst performance.

(a) Torque and Thrust Coefficients (b) Residuals

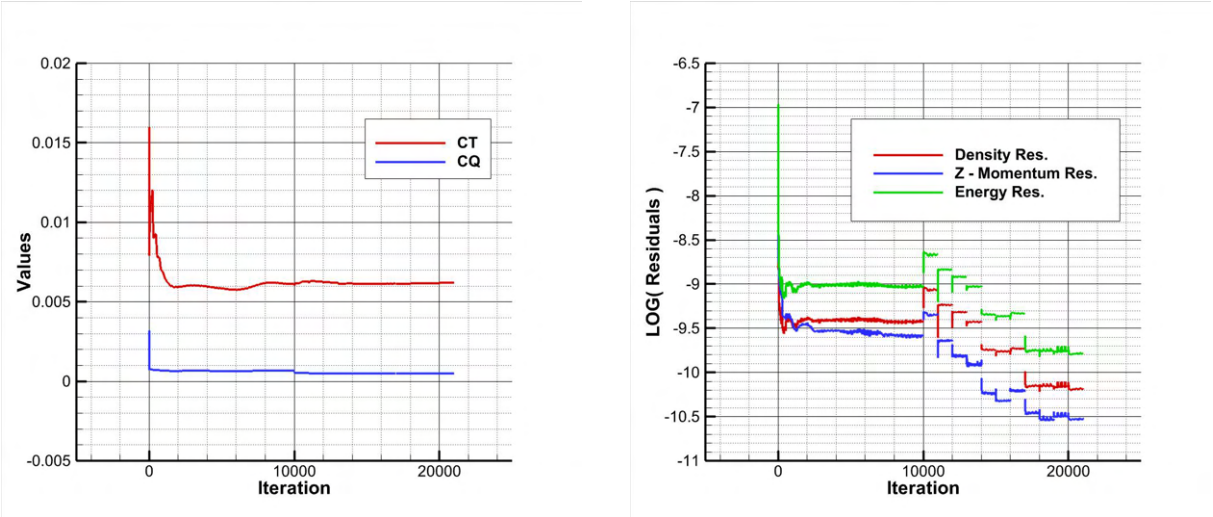

Figure 16: Variation of the analysis parameters of simulation 3 depending on the time iteration where every 1000 iterations correspond to one revolution.

Table 7: Comparison of the results with experiments by Balch and Lombardi [Balch and Lombardi, 1985]

	C_T		C_Q		FM	
	Value	% Error	Value	% Error	Value	% Error
Simulation 1	0.006268	5.4	0.000451	4.2	0.77792	13.1
Simulation 2	0.006264	5.4	0.000461	2.1	0.7602	10.5
Simulation 3	0.006195	4.2	0.000486	3.1	0.70954	3.1

CONCLUSIONS

The present study is aiming to carry out the hover analysis by implementing an AMR process. For this purpose, the SU2 software with the pyAMG library was utilized to analyze the hover performance of main rotor of the S-76 helicopter. The pyAMG library provided anisotropic mesh adaptation. Benefiting from the pyAMG, the solutions of flow-field around the S76 main rotor were conducted on significantly lower numbers of vertex in the computational domain than the studies at literature. Also, three different cases have been prepared to analyze the effects of adaptation parameters on solution. Resulting conclusions can be summarized as below.

- Resulting Grid Structures:
  - Mach sensor provided the least amount of grid numbers. However it could capture only the tip vortices.
  - Entropy sensor with HGRAD 1.2 provided the largest amount of grid. Therefore, the analysis time was increased significantly. However, it could capture the wake layer and tip vortices were captured better than the Mach sensor.
  - Entropy sensor with HGRAD 1.3 provided a grid number similar to Mach sensor. In addition, it could capture the wake layer. However, it degraded the resolution of tip vortices in the vertical direction.

- Resulting Tip Vortices:
  - Mach sensor could only capture the tip vortices. There can be seen four vortex core in the revolution 21 for this case.
  - Entropy sensor with HGRAD 1.2 captured the wake layer and gave the best resolution for the tip vortices.
  - Entropy sensor with HGRAD 1.3 provided better resolution than the Mach sensor. However its vortex structures are stretched and take a shape like a shear layer.
- Resulting Performance Parameters:
  - Mach sensor had the worst results. The second most accurate solution was provided by Entropy sensor with HGRAD 1.2. And Entropy sensor with HGRAD 1.3 showed a great conformity to the experimental results. The results and error values compared to the experimental values can be seen in Table 7. Therefore, it can be concluded that the accuracy of the performance parameters depends on wake layer in a high degree.

As an additional comment, the wake formation under the rotor loses its steadiness as moving away from the rotor. It becomes highly time-dependent at these regions (far away under the rotor). Since the mesh adaptation was applied every 1000 iterations, tip-vortices at these regions could not be captured correctly. This phenomena can be observed by looking at the entropy contours in Figures 7, 11 and 15. As seen in the Figures, the flow at regions close to the rotor could maintain its periodic nature and, so, the refinement was correct at these regions. However, it lost the periodicity far away from the rotor.

References

Abras, J., and Hariharan, N. *Comparison of CFD hover predictions on the S-76 rotor,* In 53rd AIAA Aerospace Sciences Meeting, pp. 1711, 2015

Balch, D., and Lombardi, J. *Experimental study of main rotor tip geometry and tail rotor interactions in hover. Volume 1. Text and figures*, 1985

Chaderjian, N. *Advances in rotor performance and turbulent wake simulation using DES and adaptive mesh refinement,* Seventh International Conference on Computational Fluid Dynamics (ICCFD7), 2012

Economon, T., Palacios, F., Copeland, S., Lukaczyk, T., and Alonso, J. *SU2: An open-source suite for multiphysics simulation and design,* AIAA Journal, Vol. 54, No. 3, p: 828–843, 2016

Habashi, W. G., Dompierre, J., Bourgault, Y., Ait-Ali-Yahia, D., Fortin, M., and Vallet, M.G. *Anisotropic mesh adaptation: towards user-independent, mesh-independent and solver-independent CFD. Part I: general principles,* International Journal for Numerical Methods in Fluids, Vol. 32, No. 6, p: 725–744, 2000

Hariharan, N., and Sankar, L. *A review of computational techniques for rotor wake modeling,* 38th Aerospace Sciences Meeting and Exhibit, pp. 114, 2000

Jain, R. *Hover predictions for the S-76 rotor with tip shape variation using CREATE-AV Helios,* 53rd AIAA Aerospace Sciences Meeting, pp. 1244, 2015

Jain, R. *A comparison of CFD hover predictions for the Sikorsky S-76 rotor,* 54th AIAA Aerospace Sciences Meeting, pp. 0033, 2016

Jameson, A., and Shankaran, S. *An assessment of dual-time stepping, time spectral and artificial compressibility based numerical algorithms for unsteady flow with applications to flapping wings,* 19th AIAA Computational Fluid Dynamics, p. 4273, 2009

Kang, H. J., and Kwon, O. J. *Unstructured Mesh Navier-Stokes Calculations of the Flow Field of a Helicopter Rotor in Hover,* Journal of the American Helicopter Society, Vol. 47, No. 2, p: 90–99, 2002

Narducci, R. *Hover performance assessment of several tip shapes using OVERFLOW,* 53rd AIAA Aerospace Sciences Meeting, pp. 1243, 2015

Palacios, F., Alonso, J., Duraisamy, K., Colonno, M., Hicken, J., Aranake, A., Campos, A., Copeland, S., Economon, T., Lonkar, A., and others. *Stanford University Unstructured (SU 2): An open-source integrated computational environment for multi-physics simulation and design,* 51st AIAA Aerospace Sciences Meeting including the New Horizons Forum and Aerospace Exposition, pp. 287, 2013

Palacios, F., and Economon, T. (2014). *Stanford University Unstructured (SU2): Open-Source Analysis and Design Technology for Turbulent Flows,* 52nd AIAA Aerospace Sciences, National Harbor, Madrid, 2014

"PYAMG", (2018). URL https://pyamg.saclay.inria.fr/pyamg.html.

Roe, P. L.(1981) *Approximate riemann solvers, parameter vectors, and difference schemes,* Journal of Computational Physics, Vol.43, p: 357-372, 1981

Tadghighi, H. *Helios simulation of rotors in hover: The Boeing company,* 52nd Aerospace Sciences Meeting, pp. 0209, 2014

Van Leer, B. *Towards the ultimate conservative difference scheme. V. A second-order sequel to Godunov's method,* Journal of computational Physics, Vol.32, No.1, p:101–136, 1979